Nanoscale distribution of Pb in monazite revealed by atom probe microscopy

D. Fougerouse[1,2], S.M. Reddy[1,2], D.W. Saxey[2,3], T. Erickson[1,4], C.L. Kirkland[1], W.D.A. Rickard[2,3], A.-M. Seydoux-Guillaume[5,6], C. Clark[1], I.S. Buick[7]

[1]School of Earth and Planetary Sciences, The Institute for Geoscience Research (TIGeR), Curtin University, GPO Box U1987, Perth, WA 6845, Australia.

[2]Geoscience Atom Probe, Advanced Resource Characterisation Facility, John de Laeter Centre, Curtin University, GPO Box U1987, Perth, WA 6845, Australia

[3]Department of Physics and Astronomy, Curtin University, GPO Box U1987, Perth, WA 6845, Australia

[4]Lunar and Planetary Institute, Universities Space Research Association, 3600 Bay Area Boulevard, Houston, TX, 77058, USA

[5]Université de Lyon, UJM-Saint-Etienne, UCA, CNRS, IRD, LMV UMR 6524, F-42023 Saint-Etienne, France

[6]CNRS, Université Clermont Auvergne, IRD, OPGC, Laboratoire Magmas et Volcans, F-63000 Clermont-Ferrand, France

[7]Department of Earth Sciences, Stellenbosch University, Matieland Private Bag X1, Stellenbosch, South Africa

Abstract

The widespread use of monazite ($LREEPO_4$) in U-Pb geochronology is underpinned by the assumption that it incorporates negligible amounts of Pb during initial growth, and that radiogenic Pb remains immobile after formation. We have investigated the nanoscale distribution of Pb in monazite from granulite facies rocks of the Sandmata Metamorphic Complex (Rajasthan, India) by atom probe microscopy to further understand the utility of monazite as a geochronometer. The studied monazite contains distinct 10 nm clusters,

enriched in Ca and with a bulk composition consistent with them being apatite ($Ca_5(PO_4)_3(OH)$), that are also enriched in Si and Pb relative to the monazite host. The $^{208}Pb/^{232}Th$ ratios of the clusters ranged from 1.1 ± 0.1 to 1.4 ± 0.2 (2σ), indicating that the clusters hold unsupported Pb. The $^{208}Pb/^{232}Th$ ratios of the whole specimen (including clusters) and the matrix alone are similar (<6% difference), indicating that the clusters formed shortly after monazite crystallisation by a phase exsolution mechanism that partitioned the initial common Pb and the minor radiogenic Pb into apatite. A volume-dependent analysis of the bulk monazite composition shows that a large variability in the Ca and, by proxy, Pb composition at small volumes (125 to 10,000 nm^3) due to its heterogeneous distribution in the clusters, may have detrimental effects on radiometric dating with small analytical volumes. At larger volumes, including those used in EPMA and traditional isotopic dating methods (LA-ICPMS, SIMS), the variability of Pb content is negligible. However, the measured composition may result from the mixing of multiple reservoirs.

Introduction

Monazite is a light rare earth element phosphate ($LREEPO_4$) widely used in the geosciences to date geological events. Monazite has been used to date the timing of diagenesis (Evans et al., 2002; Rasmussen et al., 2001), low-grade metamorphism (Del Río et al., 2009; Janots et al., 2008), high-grade metamorphism (e.g. (Ayers et al., 2002; Kelly et al., 2012; Laurent et al., 2016), stages of deformation during complex tectonic histories (Kirkland et al., 2016; Williams et al., 1999) and the timing of fluid movement on major structures (Kirkland et al., 2009).

Underpinning the widespread geochronological use of monazite is its ability to incorporate U and Th, but generally exclude Pb within its crystal structure during growth so there is little initial Pb (Parrish, 1990). In many circumstances, essentially all Pb in monazite can be related to radioactive decay of U and Th, which presents an ideal case for U-Pb geochronology. However, some studies have reported significant initial Pb fractions in monazite (Didier et al., 2013; Janots and Rubatto, 2014; Mottram et al., 2014; Seydoux-Guillaume et al., 2012)

indicating that a non-radiogenic Pb component can be present. The nature and the mechanisms of incorporation of this initial Pb in monazite has not been extensively studied. Previous studies have suggested that initial Pb in monazite is due to surface contamination during sample preparation, the presence of Pb in cracks and inclusions or the mixing of nanoscale Pb reservoirs (Grand'Homme et al., 2016; Seydoux-Guillaume et al., 2003).

Another assumption for the use of monazite in U-Th-Pb geochronology is that Pb produced by the radioactive decay of U and Th remains immobile, or "trapped" in the crystal lattice and that the isotopic parent-daughter pair remains coupled at the scale of the analytical volume. However, discordance is has been observed in monazite from polymetamorphic terrains indicating that Pb can be mobile at a scale of >10 µm (Bingen and van Breemen, 1998; Cocherie et al., 1998). The mechanisms responsible for Pb mobility in minerals operate at the nanoscale (Grand'Homme et al., 2017; Grand'Homme et al., 2016; Seydoux-Guillaume et al., 2003). However, such mechanisms have been previously inferred only from comparatively large scale analytical volumes (Crowley and Ghent, 1999; Goncalves et al., 2005; Paquette and Tiepolo, 2007; Tilton, 1960). In this paper, atom probe microscopy (APM) is used to investigate the nanoscale dissemination of Pb in a monazite grain to provide insight into common Pb distribution and solid state Pb mobility. APM has the unique ability to accurately measure the trace element and isotopic composition of minerals in three-dimensions and at sub-nanometre resolution as demonstrated in zircon (Peterman et al., 2016; Valley et al., 2014; Valley et al., 2015) and baddeleyite (White et al., 2017). This study focusses on the distribution of Pb in two low strain (<0.5° misorientation; fig. 1) Paleoproterozoic domains of the monazite studied by Erickson et al. (2015). These domains are characterised by low fractions of initial ^{206}Pb ranging between 0.08 and 0.73% (Erickson et al., 2015; their data repository).

The studied monazite grain comes from granulite-facies rocks of the Sandmata Complex, Rajasthan, India (Fig.1). The host rock has experienced two high-temperature metamorphic events. $M1_{SC}$ records conditions of ~7–10 kbar and 800–900 ºC and has been dated at ~1720 Ma, whilst the ~1000 Ma $M2_{SC}$ event took place at ~5–7 kbar and 600–750 ºC (Buick et al.,

2006). Monazite grains within the matrix of the studied sample record a complex Mesoproterozoic age distribution, as determined by U-Th-Pb radiometric dating, with peaks at ca. 1700 Ma and 1200 Ma, and minor Neoproterozoic ages at ca. 900 Ma (Buick et al., 2010). Electron Backscattered Diffraction (EBSD) data and correlated secondary ion mass spectrometry (SIMS) U/Pb analyses reveal systematic Pb-loss with progressive lattice strain and complete age-resetting in neoblasts formed by dynamic recrystallization at 970 ± 14 Ma (2σ, n = 6, MSWD = 1.3; Erickson et al., 2015), within error of the age of amphibolite-facies metamorphism from the adjacent Mangalwar Complex (Buick et al., 2006).

Methods

Focused ion beam. Site specific sample preparation for atom probe needle-shaped specimen was performed using the Tescan Lyra3 dual Focused Ion Beam Scanning Electron Microscope (FIB-SEM) at Curtin University using the lift-out method described in detail elsewhere (Thompson et al., 2007). The Ga^+ beam was operated at 30kV for the lift out and atom probe needle shaping, with low voltage (5kV) being used for a final polishing stage to remove effects of surface knock-on damage created by the high energy Ga beam. The same instrument, fitted with an Oxford Instruments X-max EDS detector, was used for the energy dispersive x-ray (EDS) measurements of the composition of the monazite, using an accelerating voltage of 20 keV and beam current of 1 nA. Three EDS point analyses (500,000 counts each) were performed on homogenous flat polished regions adjacent to the atom probe lift-out. The EDS data was analysed using Oxford AZtec software. Quantification results were normalised to 100 at.% with oxygen calculated by stoichiometry (2 ions). The trace elements Tb, Li, Y, U and Pb were below the detection limit of EDS and as such were not included in the quantification. Uncertainties were determined as two standard deviations from the three analyses.

Atom probe microscopy (APM). APM utilises field evaporation of atomic or molecular species from a needle-shaped specimen which are instantly ionised and accelerated to hit a

112 position sensitive detector. All species are identified by time-of-flight mass spectrometry by
113 ranging of mass-to-charge ratio (Da) spectra (e.g., Fig. 2). Each peak in the mass spectrum
114 is identified based on mass, charge state (1+ to 3+), and relative isotopic abundances. The
115 original lateral (X, Y) location of the identified species within the specimen needle can be
116 reconstructed from the detector impact location, whilst the depth (Z location) of the atom within
117 the specimen is determined from the order in which the atoms field-evaporate.
118 Atom probe microscopy was undertaken on the Advanced Resource Characterisation
119 Facility's Geoscience Atom Probe (Cameca LEAP4000X HR) housed in the John de Laeter
120 Centre, Curtin University, Perth, Australia. The instrument was operated in laser mode with a
121 UV laser (λ = 355 nm), pulse energy of 100 pJ, pulse rate of 125 kHz, base specimen
122 temperature of 50 K and evaporation rate of 0.01 atoms/pulse. Two datasets, each of ~16
123 million ions, were collected before the specimens fractured. IVAS v3.6.12 processing software
124 was used to reconstruct and analyse the data. Ca-rich clusters were observed in the
125 reconstructed 3D data. In order to minimise cross-contamination between different
126 compositional domains, a 2.5 at.% Ca isoconcentration surface (Hellman et al., 2000) was
127 used to isolate the composition of the matrix, a 5 at.% Ca surface for the isotopic analysis of
128 the clusters. Proximity histograms representing the composition of the monazite from the
129 centre of the cluster to a maximum radius of 10 nm with a resolution of 0.5 nm increments
130 (Hellman et al., 2000) were used to investigate the composition transition between the cluster
131 and the host.
132 No instrumental drift standardisation has yet been established in atom probe microscopy. Data
133 quality, in terms of background noise, mass peak overlaps and detector saturation, is
134 assessed from the data sets themselves, with uncertainties typically comparable to those
135 arising from the counting statistics for each atomic species (Peterman et al., 2016; White et
136 al., 2017). Due to peak interferences on the thermal tail of the ThO^{++} peak, each ion type used
137 for isotopic quantification was measured using a narrow range of fixed width (0.1 Da). This
138 procedure reduces the number of counts for each ion, but provides a better basis for
139 quantitative comparison between isotopes. This method is equivalent to 'full-width' ranging

applied at a specified fraction of the peak maximum, with the reasonable assumption that the peak shapes are sufficiently similar between mass peaks within a single acquisition, and that the peaks are well above the background noise (Hudson et al., 2011).

Results

The atom probe mass-to-charge spectrum of monazite is complex due to the presence of single ion species and complicated molecular species of REEs with different charge states (Fig. 2). The compositions of the monazite derived by atom probe data are deficient in O and P and enriched in REE compared to the EDS data in the same domain (Table 1) and the expected stoichiometry for monazite. Similar discrepancies in stoichiometry have been reported in some other complex oxide phases and has been attributed to a number of potential mechanisms, including the dissociation of complex molecules during the flight path, the creation and evaporation of neutral species, and the ranging of the 16 Da peak as $^{16}O^{+}$ despite overlap with the dimer $^{16}O_2^{++}$ resulting in O underestimation (Bachhav et al., 2011; Gault et al., 2016; Karahka et al., 2015; Saxey, 2011).

Despite the complexity of the spectrum, the $^{206}Pb^{++}$ and $^{208}Pb^{++}$ peaks are clearly identifiable above the background noise at 103 Da and 104 Da respectively (Fig. 2, inlay). However, the minor ^{206}Pb signal and relatively high background levels introduce a large uncertainty in its quantification and for this reason we have not reported ^{206}Pb values. No peaks were identifiable for ^{204}Pb and ^{207}Pb and therefore are not quantified in this study. Th has been quantified using four different peaks, primarily as ThO^{++} (~120 Da), but also as $ThPO_3^{+++}$ (~103.7 Da), $ThPO_4^{++}$ (~163.5 Da) and as $ThP_2O_6^{+++}$ (~195 Da). Interference of the ThO^{++} peak tail is caused by P_5O_5REE molecules (Fig. 2) altering the precise quantification of the Th concentration, and inevitably leading to the underestimation of the total Th content. $^{238}UO_2^{++}$ has been identified at mass 135 Da, however $^{235}UO_2^{++}$ is below the detection limit of our analysis and cannot be quantified. The $^{208}Pb/^{232}Th$ ratios measured from the whole specimen and matrix domain are elevated when compared to the expected age of the studied grain

(Erickson et al., 2015) because the APM measurement appears to have underestimated the Th content of the monazite. The presence of initial Pb would also increase this ratio.

The atom probe results reveal the presence of ~10 nm diameter clusters enriched in Ca, Si and Pb in a homogeneous matrix for both datasets (Fig. 3, 4). The proximity histogram profile for the largest cluster defined by a 1.3 at.% Ca isoconcentration surface (Fig. 4) shows a gradual compositional change over several nanometres with an increase of Ca, Si and Pb and decrease of O, P and REE. As shown on the proxigram (Fig. 4C), the Ca concentration varies from 1 at.% outside of the cluster to ~10 at.% in the centremost domain of the cluster. Pb and Si exhibit the same trends with an increase superior to one order of magnitude in the cluster compared to the matrix. Conversely, all other element abundances decrease in the clusters (Fig. 4, table 1). Notably, the O content decreases by ~3 at % and P by ~2 at.%. Th does not show any clear trend with values in the same range between the different domains. No F or Cl was measured in the clusters or matrix and the presence of background H in the atom probe analysis chamber precludes the discrimination of oxygen isotope peaks and overlapping hydroxyl and water molecules.

In specimen 1 the Isotopic composition of the clusters defined by a 2.5 at.% isosurface has a $^{208}Pb/^{232}Th$ ratio of 1.1 ± 0.1 (1σ) In contrast, the matrix has a $^{208}Pb/^{232}Th$ ratio of 0.1304 ± 0.0016 and the whole specimen, including the matrix and clusters, yields a $^{208}Pb/^{232}Th$ ratio of 0.1384 ± 0.0016. In specimen 1 the difference between the $^{208}Pb/^{232}Th$ ratio in the whole specimen and the matrix is 6 ± 2 %.

In specimen 2 the $^{208}Pb/^{232}Th$ ratio is 1.4 ± 0.2 (1σ) for the clusters, 0.1152 ± 0.0015 for the matrix and 0.1178 ± 0.0015 for the whole specimen. In this specimen the $^{208}Pb/^{232}Th$ ratios are within error between the whole specimen and the matrix, but the difference between absolute values is 2 ± 2 %.

Discussion

Nanoscale compositional heterogeneities in monazite

194 The reconstructed atom probe data show variations in major and trace element distribution.
195 These variations are manifest as clusters that are depleted in O, P and REEs and enriched in
196 Ca, Pb and Si. Similar nanoscale clusters were observed in monazite by transmission electron
197 microscopy (TEM) and were suggested to be a Pb-Ca-Si-O phase such as margarosanite
198 ($Ca_2PbSi_3O_9$), represent material that crystallized in fluid inclusions, or be a local domain in
199 the monazite structure, high in Pb, like the brabantite ($CaTh(PO_4)_2$) end member (Seydoux-
200 Guillaume et al., 2003). The chemical composition of the clusters measured by APM with ~10
201 at.% Ca, ~1 at.% Si and ~0.7 at.% Pb is however inconsistent with this interpretation.
202 The composition of the clusters is significantly different than the monazite host (O, P and REE
203 decrease by a few at.% whereas Ca increases by ~9 at.%), and is more consistent with apatite
204 $Ca_5(PO_4)_3(OH, Cl, F)$. Pb and Si can substitute for Ca in apatite (Harrison et al., 2002; Rønsbo,
205 1989) and can account for the increased Si and Pb content of the clusters as observed in our
206 APM data. The gradual compositional change between the two domains is also consistent
207 with the interpretation that the cluster represent nano-scale inclusions (Fougerouse et al.,
208 2016; Vurpillot et al., 2000).
209
210 *Timing of inclusion formation*
211 Different models have been proposed for the formation of nano-inclusions. These include
212 formation during annealing of radiation damages (Valley et al., 2014), dissolution-
213 reprecipitation (Harlov et al., 2011), fluid supersaturation at the crystal/fluid interface (Gebauer
214 et al., 2014; Markov, 2003) or phase immiscibility (Ferraris et al., 2005; Putnis, 1992). To
215 discriminate between these potential models it is useful to consider the mobility of Pb
216 associated with cluster formation and the timing of this mobility.
217 Previous studies investigating Pb mobility in zircons have concluded that radiation damage
218 and metamictization of the crystal structure is a prerequisite for Pb mobility and formation of
219 Pb-enriched clusters during high temperature metamorphism (Peterman et al., 2016; Valley
220 et al., 2014; Valley et al., 2015). However, the fast annealing of radiation damage in monazite
221 precludes the formation of metamict domains (Meldrum et al., 1998; Seydoux-Guillaume et

al., 2002b) which could have enhanced Pb mobility. Pb diffusion in monazite is extremely slow and almost negligible at temperatures of ~1050 ºC (Cherniak and Pyle, 2008; Cherniak et al., 2004; Gardés et al., 2006; Gardés et al., 2007; Harrison et al., 2002). Hence, volume diffusion is unlikely to be responsible for the segregation of Pb into already existing apatite nanoinclusions and therefore, Pb mobility and formation of apatite nanoinclusions are likely to be coupled.

The Sandmata rock sample studied here does not record a significant hydrous retrograde metamorphic assemblage and has remained in a dry environment since granulite facies metamorphism and initial crystallisation of the monazite (Buick et al., 2006; Buick et al., 2010; Erickson et al., 2015). The chemical zonation of the monazite (Erickson et al., 2015, their Fig. 2), including preservation of epitaxial growth zoning, is therefore not consistent with either dissolution-reprecipitation (Erickson et al., 2016) or supersaturation of the fluid at the crystal/liquid interface (Gebauer et al., 2014; Markov, 2003) .

The phase immiscibility model is based on a potential miscibility gap of Ca in monazite similar to the miscibility gap between monazite and xenotime (Andrehs and Heinrich, 1998; Gratz and Heinrich, 1997; Heinrich et al., 1997; Seydoux-Guillaume et al., 2002a). Ca can be incorporated in the monazite structure by the brabantite/cheralite coupled substitution (Ca^{2+} or Pb^{2+} + Th^{4+} or U^{4+} = $2REE^{3+}$; (Clavier et al., 2011; Spear and Pyle, 2002)). Excess Ca impurities can be assimilated in large quantities during rapid crystal growth favouring exsolution (unmixing) during slow cooling (Ferraris et al., 2005; Putnis, 1992; Watson, 1996; Watson and Liang, 1995), or during subsequent heating after a fast cooling (Putnis, 1978).

In both of our samples, the $^{208}Pb/^{232}Th$ ratio of the whole specimen and the matrix alone has a slight, but measurable difference of 6 ± 2 % in specimen 1 but are within uncertainty in specimen 2. This similarity between the two domains indicates that only a short time elapsed before the formation of the clusters. Our isotopic data are therefore in agreement with the formation of the inclusions by exsolution during the slow cooling of the Sandmata rocks, shortly after monazite crystallisation.

This finding is different to that reported in previous studies in zircon were Pb mobility was linked to a metamorphic event several hundred million years after crystallisation (Peterman et al., 2016; Valley et al., 2014; Valley et al., 2015). In our sample, this similar isotopic ratio between whole specimen and matrix indicates that the $M2_{SC}$ 600-750 °C metamorphic event at 1 Ga, some 700 Ma after monazite crystallisation cannot be responsible for the cluster formation. Hence the Pb mobility associated with neoblast formation during deformation, as documented by Erickson et al. (2015), represents a temporally distinct process from the segregation of Pb-enriched apatite inclusions.

The studied monazite grain hosts up to 0.73% initial ^{206}Pb (Erickson et al., 2015). This initial Pb value is lower than the ~6% difference between the $^{208}Pb/^{232}Th$ ratio of the whole specimen and matrix alone indicating that the Pb in the inclusions is a combination of initial Pb and radiogenic Pb produced before they formed. Additional radiogenic ^{208}Pb, would also be produced within the inclusion from the decay of inclusion-hosted Th (Table 1).

Geochronological Implications of Nanocluster in Monazite

The presence of initial Pb in nanoscale inclusions in monazite has the potential to be detrimental for geochronology depending on their concentration and the scale of the analyses. If uncorrected, the presence of unsupported Pb would increase the calculated age. There are, for instance, no common Pb correction protocols for U-Th-Pb chemical dating using electron microprobe (EPMA; Montel et al., 1996). Common Pb correction protocols exist for some dating methods based on isotopic analyses (Andersen, 2002; Ludwig, 2003), but these methods assume a homogeneous common Pb distribution and the common Pb composition at the time of incorporation. The isotopic composition of common Pb is frequently estimated using the expected composition at the age of crystallization, based on a Pb evolution model for the Earth (Stacey and Kramers, 1975), or projected using a free regression through the uncorrected data in a Tera Wasserburg diagram (Williams, 1998).

The atom probe data reveals the presence of Pb clusters composed of initial Pb and radiogenic Pb. The geochronological significance of the Pb bearing nanoclusters identified by

APM has been investigated using a spatial and statistical analysis of the 3D APM data set. In this analysis the Ca content has been used as a proxy for Pb as it provides a better signal-to-noise ratio and a more robust estimation of the effect of the nanoinclusions. Cubic volumes of varying size (125 nm^3 to 150,000 nm^3) were sampled and analysed at evenly-spaced locations throughout the three-dimensional atom probe data. Volumes composed of Ca concentrations greater than the average Ca content of the monazite indicate the presence of a cluster (or portion of one) within this volume, and hence also, a higher fraction of Pb. The Ca concentration measurements, as a function of the cubic sampling volume (Fig. 5) indicate a large variability in the Ca concentration for small sampling volumes, with values up to 20 at.% Ca. This highlights the heterogeneity of Ca throughout the analysed material and the dependence of measured values on the size of the analysis volume. By proxy, the Pb content is also highly variable for small volumes and becomes decoupled from radioactive parents. This variability decreases and is analytically negligible for sampling volumes greater than 100,000 nm^3 (10^{-4} μm^3).

Based on the size and the distribution of the clusters in the Sandmata monazite, our study predicts that for analytical volumes used for commonplace dating methods such as Electron microprobe (EPMA; ~0.5 μm^3), Secondary Ion Mass Spectrometry (SIMS; ~250 μm^3) and Laser Ablation Inductively Coupled Plasma Mass Spectrometry (LA-ICP-MS; 20,000 μm^3), the variability in the Pb fraction is negligible, as a sufficient quantity of clusters will have been incorporated into the analytical volume to result in an average Pb concentration. However, these analyses represent the mixing of multiple, discrete Pb isotopic reservoirs that do not permit the initial Pb component present in the clusters to be accurately measured or corrected.

Conclusion

This research presents detailed trace element and isotopic compositional measurements of monazite at the nanoscale to yield unique information about this widely used geochronometer. We observed 10 nm apatite nano-inclusions in monazite which formed shortly after monazite crystallisation and contain both initial Pb and radiogenic Pb. The inclusions formed by

exsolution of a Ca-bearing phase during the cooling of the rock and gathered excess Pb and Si from the monazite hosts. The inclusions spatial distribution and size control the amount of Pb signal that may end up in a given analytical volume. In the case of this monazite a negligible variability of inclusion load is found at analytical volumes >100,000 nm^3. Atom probe microscopy provides a unique and complementary tool for characterising sub-micron elemental and isotopic variations in Pb distribution within monazite.

Acknowledgements

The authors would like to acknowledge constructive reviews by Fermando Corfu, an anonymous reviewer and editorial handling by Catherine Chauvel. The Australian Resource Characterisation Facility (ARCF), under the auspices of the National Resource Sciences Precinct (NRSP) – a collaboration between CSIRO, Curtin University and The University of Western Australia – is supported by the Science and Industry Endowment Fund (SIEF RI13-01). ISB acknowledges funding under the NRF (South Africa) Incentives for Rated Researchers Scheme.

References

Andersen, T. (2002) Correction of common lead in U–Pb analyses that do not report 204 Pb. Chemical geology, 192(1), 59-79.

Andrehs, G., and Heinrich, W. (1998) Experimental determination of REE distributions between monazite and xenotime: potential for temperature-calibrated geochronology. Chemical Geology, 149(1), 83-96.

Ayers, J.C., Dunkle, S., Gao, S., and Miller, C.F. (2002) Constraints on timing of peak and retrograde metamorphism in the Dabie Shan ultrahigh-pressure metamorphic belt, east-central China, using U–Th–Pb dating of zircon and monazite. Chemical Geology, 186(3), 315-331.

Bachhav, M., Danoix, R., Danoix, F., Hannoyer, B., Ogale, S., and Vurpillot, F. (2011) Investigation of wüstite (Fe 1− x O) by femtosecond laser assisted atom probe tomography. Ultramicroscopy, 111(6), 584-588.

Bingen, B., and van Breemen, O. (1998) U-Pb monazite ages in amphibolite-to granulite-facies orthogneiss reflect hydrous mineral breakdown reactions: Sveconorwegian Province of SW Norway. Contributions to Mineralogy and Petrology, 132(4), 336-353.

Buick, I., Allen, C., Pandit, M., Rubatto, D., and Hermann, J. (2006) The Proterozoic magmatic and metamorphic history of the Banded Gneiss Complex, central Rajasthan, India: LA-ICP-MS U–Pb zircon constraints. Precambrian Research, 151(1), 119-142.

Buick, I., Clark, C., Rubatto, D., Hermann, J., Pandit, M., and Hand, M. (2010) Constraints on the Proterozoic evolution of the Aravalli–Delhi Orogenic belt (NW India) from monazite geochronology and mineral trace element geochemistry. Lithos, 120(3), 511-528.

Cherniak, D., and Pyle, J. (2008) Th diffusion in monazite. Chemical Geology, 256(1), 52-61.

Cherniak, D., Watson, E.B., Grove, M., and Harrison, T.M. (2004) Pb diffusion in monazite: a combined RBS/SIMS study. Geochimica et Cosmochimica Acta, 68(4), 829-840.

Clavier, N., Podor, R., and Dacheux, N. (2011) Crystal chemistry of the monazite structure. Journal of the European Ceramic Society, 31(6), 941-976.

Cocherie, A., Legendre, O., Peucat, J., and Kouamelan, A. (1998) Geochronology of polygenetic monazites constrained by in situ electron microprobe Th-U-total lead determination: implications for lead behaviour in monazite. Geochimica et Cosmochimica Acta, 62(14), 2475-2497.

Crowley, J., and Ghent, E. (1999) An electron microprobe study of the U–Th–Pb systematics of metamorphosed monazite: the role of Pb diffusion versus overgrowth and recrystallization. Chemical Geology, 157(3), 285-302.

Del Río, P., Barbero, L., Mata, P., and Fanning, C. (2009) Timing of diagenesis and very low-grade metamorphism in the eastern sector of the Sierra de Cameros (Iberian Range, Spain): a U–Pb SHRIMP study on monazite. Terra Nova, 21(6), 438-445.

Didier, A., Bosse, V., Boulvais, P., Bouloton, J., Paquette, J.-L., Montel, J.-M., and Devidal, J.-L. (2013) Disturbance versus preservation of U–Th–Pb ages in monazite during fluid–rock interaction: textural, chemical and isotopic in situ study in microgranites (Velay Dome, France). Contributions to Mineralogy and Petrology, 165(6), 1051-1072.

Erickson, T., Pearce, M., Taylor, R., Timms, N.E., Clark, C., Reddy, S., and Buick, I. (2015) Deformed monazite yields high-temperature tectonic ages. Geology, 43(5), 383-386.

Erickson, T., Reddy, S., Timms, N., Pearce, M., Taylor, R., Clark, C., and Buick, I. (2016) Deformed monazite yields high-temperature tectonic ages: REPLY. Geology, 44(1), e378-e378.

Evans, J., Zalasiewicz, J., Fletcher, I., Rasmussen, B., and Pearce, N. (2002) Dating diagenetic monazite in mudrocks: constraining the oil window? Journal of the Geological Society, 159(6), 619-622.

Ferraris, C., White, T., Plévert, J., and Wegner, R. (2005) Nanometric modulation in apatite. Physics and chemistry of minerals, 32(7), 485-492.

Fougerouse, D., Reddy, S.M., Saxey, D.W., Rickard, W.D., Van Riessen, A., and Micklethwaite, S. (2016) Nanoscale gold clusters in arsenopyrite controlled by growth rate not concentration: Evidence from atom probe microscopy. American Mineralogist, 101(8), 1916-1919.

Gardés, E., Jaoul, O., Montel, J.-M., Seydoux-Guillaume, A.-M., and Wirth, R. (2006) Pb diffusion in monazite: An experimental study of Pb2++ Th4+⇔ 2Nd3+ interdiffusion. Geochimica et Cosmochimica Acta, 70(9), 2325-2336.

Gardés, E., Montel, J.-M., Seydoux-Guillaume, A.-M., and Wirth, R. (2007) Pb diffusion in monazite: New constraints from the experimental study of Pb2+⇔ Ca2+ interdiffusion. Geochimica et Cosmochimica Acta, 71(16), 4036-4043.

386 Gault, B., Saxey, D.W., Ashton, M.W., Sinnott, S.B., Chiaramonti, A.N., Moody, M.P., and
387 Schreiber, D.K. (2016) Behavior of molecules and molecular ions near a field emitter.
388 New Journal of Physics, 18(3), 033031.
389 Gebauer, D., Kellermeier, M., Gale, J.D., Bergström, L., and Cölfen, H. (2014) Pre-
390 nucleation clusters as solute precursors in crystallisation. Chemical Society Reviews,
391 43(7), 2348-2371.
392 Goncalves, P., Williams, M.L., and Jercinovic, M.J. (2005) Electron-microprobe age mapping
393 of monazite. American Mineralogist, 90(4), 578-585.
394 Grand'Homme, A., Janots, E., Seydoux-Guillaume, A.M., Guillaume, D., Magnin, V.,
395 Hövelmann, J., Höschen, C., and Boiron, M.C. (2017) Mass transport and
396 fractionation during monazite alteration by anisotropic replacement. Chemical
397 Geology.
398 Grand'Homme, A., Janots, E., Seydoux-Guillaume, A.-M., Guillaume, D., Bosse, V., and
399 Magnin, V. (2016) Partial resetting of the U-Th-Pb systems in experimentally altered
400 monazite: Nanoscale evidence of incomplete replacement. Geology, 44(6), 431-434.
401 Gratz, R., and Heinrich, W. (1997) Monazite-xenotime thermobarometry: Experimental
402 calibration of the miscibility gap in the binary system CePO4-YPO4. American
403 Mineralogist, 82(7-8), 772-780.
404 Harlov, D.E., Wirth, R., and Hetherington, C.J. (2011) Fluid-mediated partial alteration in
405 monazite: the role of coupled dissolution–reprecipitation in element redistribution and
406 mass transfer. Contributions to Mineralogy and Petrology, 162(2), 329-348.
407 Harrison, T.M., Catlos, E.J., and Montel, J.-M. (2002) U-Th-Pb dating of phosphate minerals.
408 Reviews in Mineralogy and Geochemistry, 48(1), 524-558.
409 Heinrich, W., Rehs, G., and Franz, G. (1997) Monazite–xenotime miscibility gap
410 thermometry. I. An empirical calibration. Journal of Metamorphic Geology, 15(1), 3-
411 16.

Hellman, O.C., Vandenbroucke, J.A., Rüsing, J., Isheim, D., and Seidman, D.N. (2000) Analysis of three-dimensional atom-probe data by the proximity histogram. Microscopy and Microanalysis, 6(05), 437-444.

Hudson, D., Smith, G., and Gault, B. (2011) Optimisation of mass ranging for atom probe microanalysis and application to the corrosion processes in Zr alloys. Ultramicroscopy, 111(6), 480-486.

Janots, E., Engi, M., Berger, A., Allaz, J., Schwarz, J.O., and Spandler, C. (2008) Prograde metamorphic sequence of REE minerals in pelitic rocks of the Central Alps: implications for allanite–monazite–xenotime phase relations from 250 to 610 C. Journal of Metamorphic Geology, 26(5), 509-526.

Janots, E., and Rubatto, D. (2014) U–Th–Pb dating of collision in the external Alpine domains (Urseren zone, Switzerland) using low temperature allanite and monazite. Lithos, 184, 155-166.

Karahka, M., Xia, Y., and Kreuzer, H. (2015) The mystery of missing species in atom probe tomography of composite materials. Applied Physics Letters, 107(6), 062105.

Kelly, N.M., Harley, S.L., and Möller, A. (2012) Complexity in the behavior and recrystallization of monazite during high-T metamorphism and fluid infiltration. Chemical geology, 322, 192-208.

Kirkland, C., Erickson, T., Johnson, T., Danišík, M., Evans, N., Bourdet, J., and McDonald, B. (2016) Discriminating prolonged, episodic or disturbed monazite age spectra: An example from the Kalak Nappe Complex, Arctic Norway. Chemical Geology, 424, 96-110.

Kirkland, C.L., Whitehouse, M.J., and Slagstad, T. (2009) Fluid-assisted zircon and monazite growth within a shear zone: a case study from Finnmark, Arctic Norway. Contributions to Mineralogy and Petrology, 158(5), 637-657.

Laurent, A.T., Seydoux-Guillaume, A.-M., Duchene, S., Bingen, B., Bosse, V., and Datas, L. (2016) Sulphate incorporation in monazite lattice and dating the cycle of sulphur in metamorphic belts. Contributions to Mineralogy and Petrology, 171(11), 94.

Ludwig, K.R. (2003) User's manual for Isoplot 3.00: a geochronological toolkit for Microsoft Excel. Kenneth R. Ludwig.

Markov, I.V. (2003) Crystal growth for beginners: fundamentals of nucleation, crystal growth and epitaxy. World scientific.

Meldrum, A., Boatner, L., Weber, W., and Ewing, R. (1998) Radiation damage in zircon and monazite. Geochimica et Cosmochimica Acta, 62(14), 2509-2520.

Mottram, C.M., Warren, C.J., Regis, D., Roberts, N.M., Harris, N.B., Argles, T.W., and Parrish, R.R. (2014) Developing an inverted Barrovian sequence; insights from monazite petrochronology. Earth and Planetary Science Letters, 403, 418-431.

Paquette, J.-L., and Tiepolo, M. (2007) High resolution (5 μm) U–Th–Pb isotope dating of monazite with excimer laser ablation (ELA)-ICPMS. Chemical Geology, 240(3), 222-237.

Parrish, R.R. (1990) U-Pb dating of monazite and its application to geological problems. Canadian Journal of Earth Sciences, 27(11), 1431-1450.

Peterman, E.M., Reddy, S.M., Saxey, D.W., Snoeyenbos, D.R., Rickard, W.D., Fougerouse, D., and Kylander-Clark, A.R. (2016) Nanogeochronology of discordant zircon measured by atom probe microscopy of Pb-enriched dislocation loops. Science Advances, 2(9), e1601318.

Putnis, A. (1978) The mechanism of exsolution of hematite from iron-bearing rutile. Physics and Chemistry of Minerals, 3(2), 183-197.

Putnis, A. (1992) An introduction to mineral sciences. Cambridge University Press.

Rasmussen, B., Fletcher, I.R., and McNaughton, N.J. (2001) Dating low-grade metamorphic events by SHRIMP U-Pb analysis of monazite in shales. Geology, 29(10), 963-966.

Rønsbo, J. (1989) Coupled substitutions involving REEs and Na and Si in apatites in alkaline rocks from the Ilimaussaq intrusion, South Greenland, and the petrological implications. American Mineralogist, 74(7-8), 896-901.

Saxey, D. (2011) Correlated ion analysis and the interpretation of atom probe mass spectra. Ultramicroscopy, 111(6), 473-479.

Seydoux-Guillaume, A.-M., Goncalves, P., Wirth, R., and Deutsch, A. (2003) Transmission electron microscope study of polyphase and discordant monazites: Site-specific specimen preparation using the focused ion beam technique. Geology, 31(11), 973-976.

Seydoux-Guillaume, A.-M., Montel, J.-M., Bingen, B., Bosse, V., De Parseval, P., Paquette, J.-L., Janots, E., and Wirth, R. (2012) Low-temperature alteration of monazite: Fluid mediated coupled dissolution–precipitation, irradiation damage, and disturbance of the U–Pb and Th–Pb chronometers. Chemical Geology, 330, 140-158.

Seydoux-Guillaume, A.-M., Wirth, R., Heinrich, W., and Montel, J.-M. (2002a) Experimental determination of thorium partitioning between monazite and xenotime using analytical electron microscopy and X-ray diffraction Rietveld analysis. European Journal of Mineralogy, 14(5), 869-878.

Seydoux-Guillaume, A.-M., Wirth, R., Nasdala, L., Gottschalk, M., Montel, J.-M., and Heinrich, W. (2002b) An XRD, TEM and Raman study of experimentally annealed natural monazite. Physics and Chemistry of Minerals, 29(4), 240-253.

Spear, F.S., and Pyle, J.M. (2002) Apatite, monazite, and xenotime in metamorphic rocks. Reviews in Mineralogy and Geochemistry, 48(1), 293-335.

Stacey, J.t., and Kramers, J. (1975) Approximation of terrestrial lead isotope evolution by a two-stage model. Earth and Planetary Science Letters, 26(2), 207-221.

Thompson, K., Lawrence, D., Larson, D., Olson, J., Kelly, T., and Gorman, B. (2007) In situ site-specific specimen preparation for atom probe tomography. Ultramicroscopy, 107(2), 131-139.

Tilton, G. (1960) Volume diffusion as a mechanism for discordant lead ages. Journal of Geophysical Research, 65(9), 2933-2945.

Valley, J.W., Cavosie, A.J., Ushikubo, T., Reinhard, D.A., Lawrence, D.F., Larson, D.J., Clifton, P.H., Kelly, T.F., Wilde, S.A., and Moser, D.E. (2014) Hadean age for a post-magma-ocean zircon confirmed by atom-probe tomography. Nature Geoscience, 7(3), 219-223.

Valley, J.W., Reinhard, D.A., Cavosie, A.J., Ushikubo, T., Lawrence, D.F., Larson, D.J., Kelly, T.F., Snoeyenbos, D.R., and Strickland, A. (2015) Presidential Address. Nano- and micro-geochronology in Hadean and Archean zircons by atom-probe tomography and SIMS: New tools for old minerals. American Mineralogist, 100(7), 1355-1377.

Vurpillot, F., Bostel, A., and Blavette, D. (2000) Trajectory overlaps and local magnification in three-dimensional atom probe. Applied Physics Letters, 76(21), 3127-3129.

Watson, E.B. (1996) Surface enrichment and trace-element uptake during crystal growth. Geochimica et Cosmochimica Acta, 60(24), 5013-5020.

Watson, E.B., and Liang, Y. (1995) A simple model for sector zoning in slowly grown crystals: Implications for growth rate and lattice diffusion, with emphasis on accessory minerals in crustal rocks. American Mineralogist, 80(11-12), 1179-1187.

White, L.F., Darling, J., Moser, D., Reinhard, D., Prosa, T., Bullen, D., Olsen, D., Larson, D., Lawrence, D., and Martin, I. (2017) Atomic-scale age resolution of planetary events. Nature Communications, 8, 1-6.

Williams, I.S. (1998) U-Th-Pb geochronology by ion microprobe. Applications of microanalytical techniques to understanding mineralizing processes, 1-35.

Williams, M.L., Jercinovic, M.J., and Terry, M.P. (1999) Age mapping and dating of monazite on the electron microprobe: Deconvoluting multistage tectonic histories. Geology, 27(11), 1023-1026.

Figures:

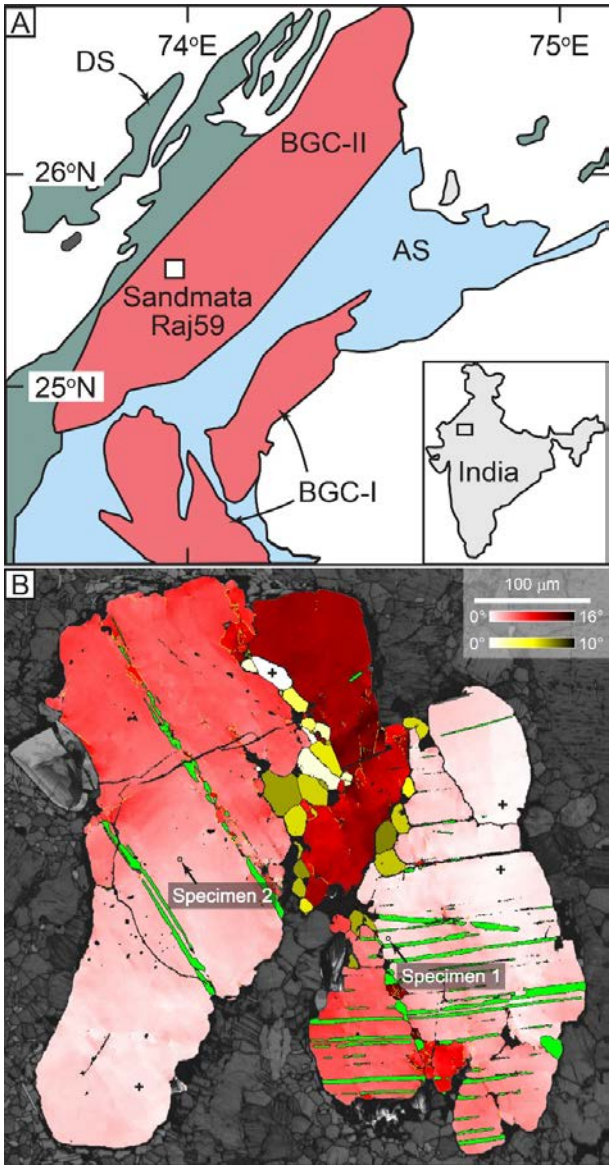

Figure 1: A) Simplified geological map of the Sandmata granulite complex indicating the location of sample Raj59 modified from Buick et al. (2010). Abbreviations: AS - Aravalli Supergroup; BGC - Banded Gneiss Complex; DS - Delhi Supergroup. B) Crystallographic orientation electron backscattered diffraction map. Misorientation in each of the host domain grains is colour coded red from a reference point "+" to maximum of 16°; Neoblasts formed by dynamic recrystallization are colour coded yellow for misorientation ranging between 0 and 10° from the reference point "+"; Low-angle grain boundaries (1°) are coloured yellow, while (001), (100) and (122) deformation twins are plotted green, modified from Erickson et al. (2015). The atom probe microscopy (APM) samples were extracted from two weakly deformed domains (<0.5°) of the crystal, marked as open circles on the figure.

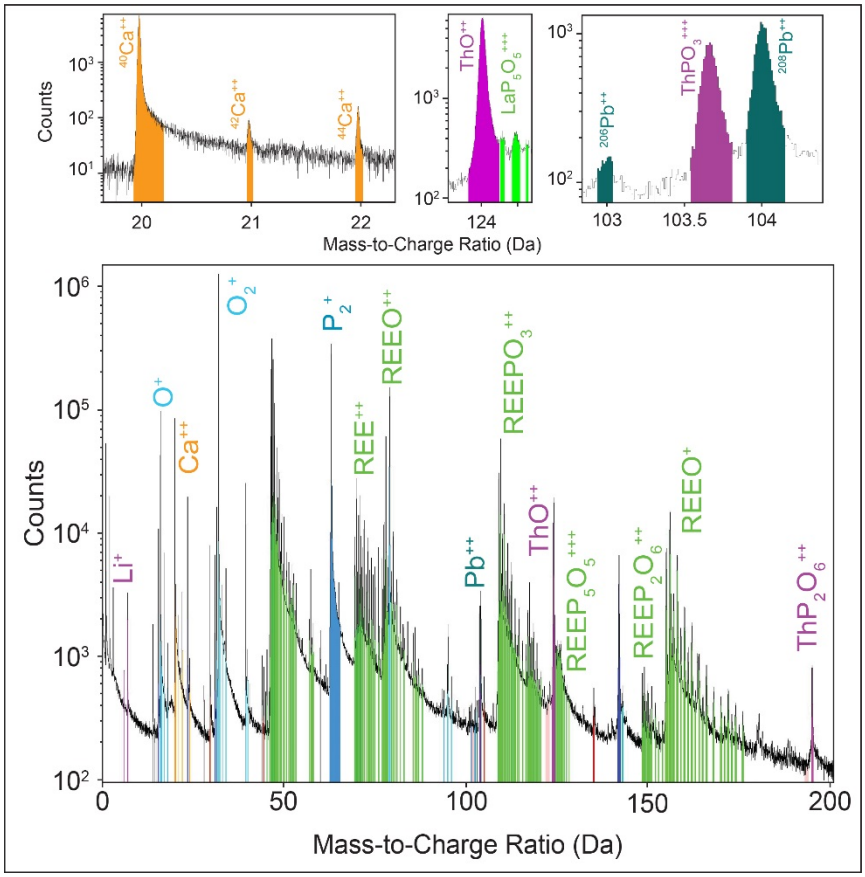

Figure 2: Atom probe mass spectrum. Peaks are color-coded by atomic or molecular species.

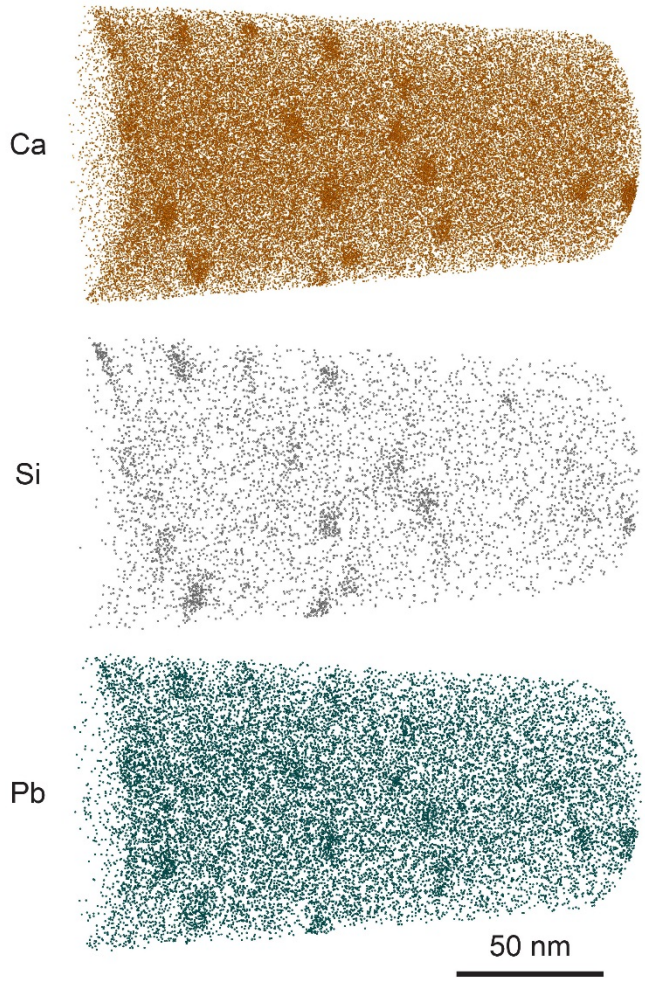

532

533 Figure 3: Specimen 1: Reconstructed three-dimensional atom probe image of Ca, Si and Pb

534 (^{206}Pb + ^{208}Pb) distribution. Each sphere represents one atom. The maps show the presence

535 of Ca-Si-Pb clusters.

536

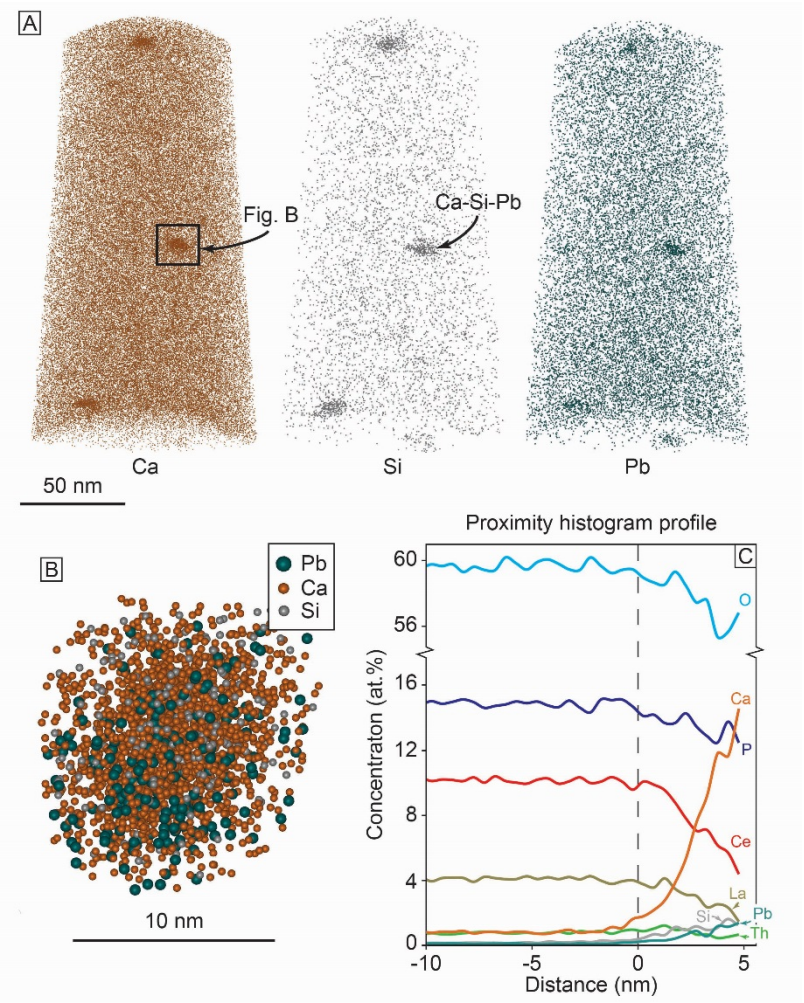

Figure 4: Specimen 2: A) Reconstructed three-dimensional atom probe image of Ca, Si and Pb (^{206}Pb + ^{208}Pb) distribution. Each sphere represents one atom. The maps show the presence of three Ca-Si-Pb clusters. B) Close up of the biggest cluster. C) Proximity histogram profile based on a 1.3 at.% Ca isosurface (distance 0 represent the edge of the isosurface). The histogram shows the decrease of O, P and REEs but the increase of Ca, Si and Pb.

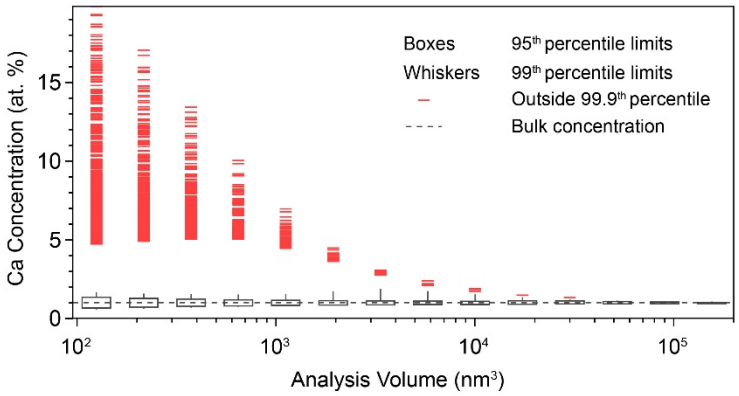

Figure 5: Box and whisker plot indicating the range of Ca concentration measurements that could be obtained depending on the scale of the cubic sampling volume applied to an APM dataset (specimen 2). Ca concentrations for volumes from 125 nm^3 to 150,000 nm^3 were generated from the three-dimensional atom probe data, by sampling cubic volumes at evenly-spaced locations throughout the data. Boxes indicate 95th percentile limits (approximately 2-sigma for Gaussian distributed data), and whiskers 99th percentile. Outliers beyond the 99.9th percentile are plotted in red for volumes up to 150,000 nm^3. Whiskers and outliers are only shown if their percentile cut-offs are compatible with the sample size. The dashed line indicates the bulk composition, calculated from the full atom probe dataset.

Table 1: Composition (major, trace and isotopic) of the different domains given by atom probe and EDX. The composition of a stoichiometric apatite is also given for reference.